*Synthesis, electronic structure and redox properties of the diruthenium sandwich complexes [Cp*Ru(μ-C10H8)RuCp*]x (x = 0, 1+; Cp* = C5Me5; C10H8 = naphthalene)*

Article

Accepted Version

Dalton Transactions

ARTICLE

Synthesis, electronic structure and redox properties of the diruthenium sandwich complexes [Cp*Ru(μ-$C_{10}H_8$)RuCp*]^x (x = 0, 1+; Cp* = C_5Me_5; $C_{10}H_8$ = naphthalene)

Received 00th January 20xx,
Accepted 00th January 20xx

DOI: 10.1039/x0xx00000x

www.rsc.org/

Dirk Herrmann,[a] Christian Rödl,[a] Bas de Bruin,[b] František Hartl[c] and Robert Wolf[a]*

The dinuclear ruthenium complex [Cp*Ru(μ-$C_{10}H_8$)RuCp*] (**1**; Cp* = η^5-C_5Me_5) was prepared by reduction of the cationic precursor [Cp*Ru(η^6-$C_{10}H_8$)]PF_6 with KC_8. Diamagnetic **1** shows a symmetric molecular structure. DFT studies showed an electronic structure similar to that of the analogous diiron complex [Cp*Fe(μ-$C_{10}H_8$)FeCp*]. Cyclic voltammetry and UV-vis spectroelectrochemistry showed that **1** can be reversibly oxidized to $\mathbf{1}^+$ and $\mathbf{1}^{2+}$. Chemical oxidation with [Cp_2Fe]BAr^F_4 afforded the paramagnetic compound [**1**]BAr^F_4, which was investigated by EPR, single-crystal X-ray diffractometry and density functional theory calculations. Reaction of **1** with Brookhart's acid gave the hydride complex [**3**]BAr^F_4, which was characterized spectroscopically and crystallographically. Cyclic voltammetry showed that [**3**]$^+$ is converted back to **1** upon reduction and oxidation.

Introduction

Hydrocarbon-bridged complexes are of potential interest as model compounds to study the electronic communication between two metal centers, which is relevant for the design of potential electronic devices.[1] In this regard, considerable attention has been directed toward the use of polyaromatic bridging ligands, which may provide a varying degree of electronic coupling between the coordinated metal atoms through their conjugated π system.[2] The two simplest polyarenes, naphthalene and anthracene, should enable a particularly strong electronic coupling between the metal atoms, yet the number of known bimetallic naphthalene and anthracene complexes is still surprisingly small. Compounds **A**–**E** (Figure 1) containing vanadium, chromium and manganese are early examples.[3] A related diiron complex, [CpFe(μ-$C_{14}H_{10}$)FeCp]$^{2+}$ (**F**$^{2+}$, $C_{14}H_{10}$ = anthracene), was prepared by Hendrickson and co-workers.[4] The group of Jonas later extended this family by synthesizing [CpFe(μ-$C_{10}H_8$)FeCp] (**H**) and [Cp*Fe(μ-$C_{10}H_8$)FeCp*] (**J**).[5] A single-crystal X-ray structure analysis of **J** confirmed the *anti*-facial arrangement of the CpFe moieties.

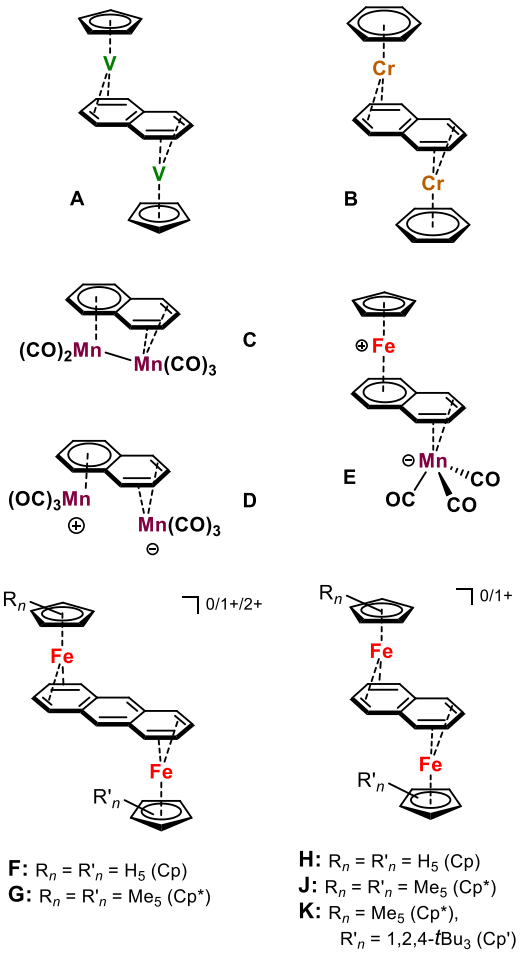

F: R_n = R'_n = H_5 (Cp)
G: R_n = R'_n = Me_5 (Cp*)

H: R_n = R'_n = H_5 (Cp)
J: R_n = R'_n = Me_5 (Cp*)
K: R_n = Me_5 (Cp*), R'_n = 1,2,4-tBu$_3$ (Cp')

Figure 1 Examples of naphthalene- and anthracene-bridged transition metal complexes.

[a] University of Regensburg, Institute of Inorganic Chemistry, 93040 Regensburg, Germany. E-Mail: robert.wolf@ur.de.
[b] University of Amsterdam, Van 't Hoff Institute for Molecular Sciences, Homogeneous and Supramolecular Catalysis, Science Park 904, 1098 XH Amsterdam, The Netherlands. E-Mail: b.debruin@uva.nl
[c] University of Reading, Department of Chemistry, Whiteknights, Reading, RG6 6AD, United Kingdom. E-Mail: f.hartl@reading.ac.uk
Electronic Supplementary Information (ESI) available: [details of any supplementary information available should be included here]. See DOI: 10.1039/x0xx00000x

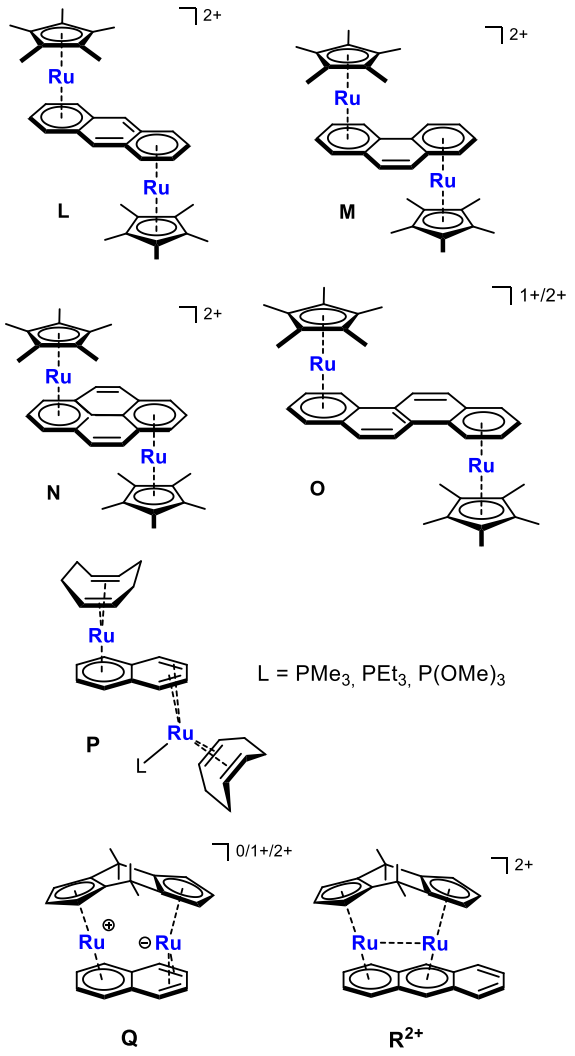

Figure 2 Previously characterized polyarene-bridged diruthenium complexes.

Polyarene-bridged complexes are also known for ruthenium and rhodium (Figure 2).[6-8] Diruthenium cations *anti*-[Cp*Ru(μ-η^6:η^6-L)RuCp*]^x (**L**-**O**, x = 1+ or 2+, L = anthracene [**L**], phenanthrene [**M**], pyrene [**N**], and chrysene [**O**]) were reported by the groups of Kölle and Román.[7a-c] A single crystal X-ray diffraction study of the chrysene complex revealed the *anti*-facial configuration of the metal centers.[7c] The μ-η^6:η^4-naphthalene diruthenium complex [(η^4-cod)Ru(μ-η^6:η^4-$C_{10}H_8$)Ru(η^4-cod)(L)] (**P**, cod = 1,5-cyclo-octadiene, L = PMe_3, PEt_3, and $P(OMe)_3$) reported by Bennett and co-workers also displays an *anti*-facial structure,[9] while Chin and co-workers recently described the *syn*-facial naphthalene and anthracene-bridged complexes **Q** and **R**$^{2+}$ (Figure 2). The *syn*-facial arrangement is due to the presence of a doubly-bridged dicyclopentadienyl ligand connecting the ruthenium atoms.[7d]

During our investigations of synthetic applications of low-valent polyarene transition metalates,[10] we became interested in the chemistry of bimetallic polyarene iron and ruthenium complexes. We discovered a new route to the previously reported diiron complex **J** (Figure 1), and we synthesized and characterized the closely related diiron complex **K** (Figure 2) and the iron-ruthenium complexes **S** and **T**.[11] In an independent study, Ohki, Tatsumi and co-workers prepared Cp*-substituted compounds **G** and **J**. Monocationic oxidation products [**F'**]BAr^F_4 and [**J**]BAr^F_4 were isolated by oxidizing the neutral precursors with $[Cp_2Fe]PF_6$ and subsequent anion exchange with $NaBAr^F_4$.[12] We similarly obtained the monocationic diiron and iron-ruthenium complexes [Cp'Fe(μ-$C_{10}H_8$)FeCp*]PF_6 ([**K**]PF_6, Cp' = C_5H_2-1,2,4-*t*Bu_3) and [Cp'Fe(μ-$C_{10}H_8$)RuCp*]PF_6 ([**T**]PF_6) by oxidizing neutral **K** and **T** with $[Cp_2Fe]PF_6$.[11c] Combined spectroscopic, electrochemical and quantum chemical studies showed that the electronic structures of such diiron and iron-ruthenium complexes are only marginally influenced by different substitution patterns on the Cp ligand (Cp* vs. Cp').[11] Interestingly, substituting one of the iron centers by ruthenium in the heterometallic complexes **S**-**T** had a modest effect as well.[11c] This observation was explained by the similar composition of the frontier molecular orbitals in the diiron and iron-ruthenium complexes, which are dominated by contributions from iron and ligand-based atomic orbitals, whereas the ruthenium-based orbitals appear to be less relevant.[11c]

In extension of these previous studies, we next sought to prepare the corresponding diruthenium complexes. Here, we report the synthesis, structural, and spectroscopic characterization of the new naphthalene-bridged complexes *anti*-[Cp*Ru(μ-$C_{10}H_8$)RuCp*] (**1**, Figure 3) and *anti*-[Cp*Ru(μ-$C_{10}H_8$)RuCp*]BAr^F_4 ([**1**]BAr^F_4). By comparing the structural and spectroscopic characteristics with DFT calculations, we now arrive at a comprehensive picture of the electronic structures of the naphthalene-bridged diiron, iron-ruthenium, and diruthenium compounds.

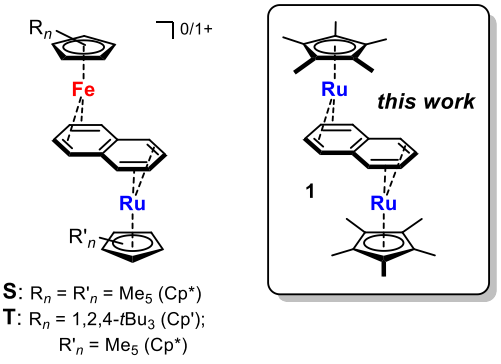

Figure 3. Naphthalene-bridged iron-ruthenium and diruthenium complexes.

Results and Discussion

Two previous studies have described reductions of the cation [Cp*Ru(η^6-$C_{10}H_8$)]$^+$ (**2**$^+$).[7a,13] In their electrochemical investigation of **2**$^+$ and related ruthenium-arene complexes, Kölle and co-workers observed a reduction of **2**$^+$ in CH_2Cl_2 at –1.96 V.† This redox event was reversible only at very high scan rates. They concluded that "short-lived neutral Cp*Ru(η^6-arene) complexes undergo decomplexation rather than dimerization or hydrogen abstraction."[7a] In a subsequent study, Gusev and co-workers observed a reversible reduction of

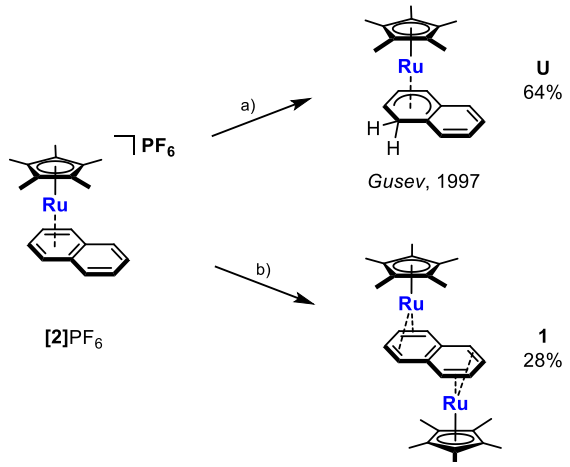

Scheme 1 Synthesis of complexes **1** and **U**;[13] conditions and reagents: a) Na/Hg (excess), THF; b) KC_8 (1.1 equiv.) / $-C_{10}H_8$, DME, 16 h, –30°C to r.t.

$\mathbf{2}^+$ in acetonitrile at –2.10 V and a second, irreversible reduction at –3.16 V. The mononuclear benzocyclohexadienyl complex [Cp*Ru($C_{10}H_9$)] (**U**) was identified as the major product of the chemical reduction of $\mathbf{2}^+$ with an excess of Na/Hg in THF (Scheme 1a).[13]

We recorded a cyclic voltammogram of [**2**]PF_6 in THF. In contrast to the previous studies in CH_2Cl_2 and acetonitrile, we observed two overlapping, reduction processes at –1.99 and –2.10 V (Figure 4), which are chemically reversible on the CV time scale. The reason for the observed splitting is not entirely clear, but a plausible explanation might be that there is an interaction between $\mathbf{2}^+$ and **2** as a first step to trigger the formation of dinuclear complex **1** (*vide infra*).

Chemical reduction of [**2**]PF_6 with potassium graphite in 1,2-dimethoxyethane (Scheme 1b) yielded the dinuclear complex [Cp*Ru(μ-$C_{10}H_8$)RuCp*] (**1**) rather than mononuclear **2**.

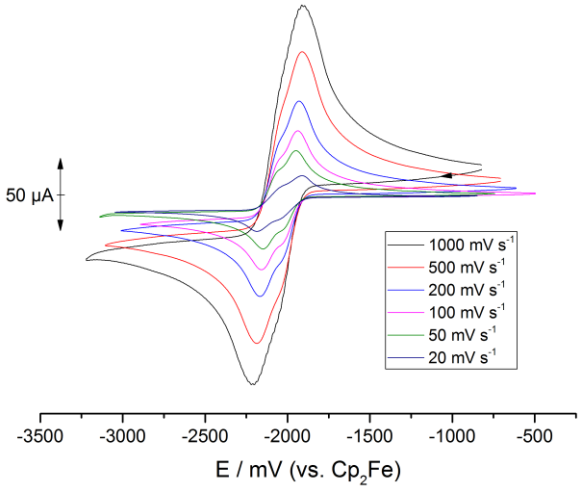

Figure 4 Cyclic voltammogram of [**2**]PF_6 in THF/NBu_4PF_6 at varying scan rates. Working electrode: Pt minidisk, counter electrode: Pt wire, pseudoreference electrode: Ag wire.

Dichroic red-green crystals of **1** were isolated in 28% yield after work-up. Compound **U** was detected as a by-product by ^{1}H NMR spectroscopy of the crude reaction mixture.

X-ray structural analysis

Complex **1** crystallizes from *n*-hexane (space group $P2_1/n$ with two molecules in the unit cell). The solid-state molecular structure is centrosymmetric and reveals an *anti*-facial configuration of the two Cp*Ru moieties that bind to opposite faces of the bridging naphthalene ligand (Figure 5). The naphthalene ligand is η^4-coordinated to both Cp*Ru units with Ru–C distances from 2.158(1) to 2.230(1) Å (Table 1), while the distances to the bridgehead carbons C15 and C15' (av. 2.589(1) Å) are substantially longer. In accord with this, the naphthalene ligand is folded by 14.6° along the C11–C14 vector. The naphthalene ligand in **1** shows very similar C11–C12, C12–C13, and C13–C14 bond lengths (see Table 1 and Figure 6) due to the back-bonding from the low-valent ruthenium centers to the ligand.[14]

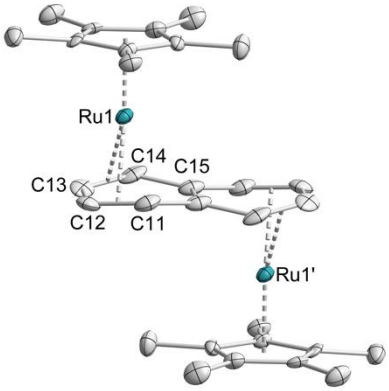

Figure 5. Solid-state X-ray structure of **1** (thermal ellipsoids at 50% probability, H atoms omitted for clarity); see Table 1 for selected bond lenghts and angles.

The structural data of **1** are comparable to those of the analogous diiron and iron-ruthenium complexes (**F–K, S** and **T**, Figures 1 and 3), which display similar centrosymmetric structures with an *anti*-facial configuration of the metal centers and essentially η^4-coordinated aromatic rings.[11b,c] It is also noteworthy that the molecular structure of **1** differs from the closely related *syn*-facial complex **Q** (Figure 2), which features an asymmetric η^4:η^6 coordination of the naphthalene ligand distinct from the symmetric structure of **1** (Ru1–C 2.180(2) to 2.336(2) Å and Ru2–C 2.136(2) to 2.190(2) Å; see Table 1 for more details).[7d] The presence of the η^4:η^6-naphthalene ligand in **Q** indicates a mixed-valent $Ru^{II}Ru^0$ electronic structure with the ruthenium atoms in d^6 and d^8 configurations, respectively. DFT calculations performed by Chin and co-workers gave an energy difference of approximately 4.7 kcal mol^{-1} between the disfavored C_{2v} symmetric structure akin to **1** and the C_s symmetric ground state.[7d]

Dalton Transactions

ARTICLE

Table 1. Selected bond lengths (Å) and angles (°) of complexes **1**, **J**, **T**, **U** and **Q** determined by X-ray crystallography and DFT (DFT values given in italics). Numbering according to Figure 6.

	1 (M^1 = M^2 = Ru)	**J** (M^1 = M^2 = Fe)	**S** (M^1 = Fe, M^2 = Ru)	**T** (M^1 = Fe, M^2 = Ru)[a]	**Q** (M^1 = M^2 = Ru)[b]
M1–C11	2.225(1) / *2.228*	2.101(2) / *2.102*	– / *2.101*	2.105(4) / *2.12*	2.190(2)
M1–C12	2.158(1) / *2.178*	2.016(3) / *2.025*	– / *2.028*	2.012(5) / *2.02*	2.136(2)
M1–C13	2.177(1) / *2.178*	2.031(3) / *2.025*	– / *2.028*	2.003(5) / *2.02*	2.136(2)
M1–C14	2.230(1) / *2.225*	2.100(3) / *2.102*	– / *2.100*	2.134(3) / *2.14*	2.177(2)
M1–C19	2.592(1) / *2.541*	2.441(2) / *2.427*	– / *2.424*	2.696(2) / *2.65*	2.901(2)
M1–C20	2.586(1) / *2.548*	2.435(2) / *2.427*	– / *2.419*	2.718(2) / *2.65*	2.885(2)
M1–C(Cp) (av.)	2.189(8)	2.068(9)	–	2.080(4) / *2.09*	2.195(3)
M2–C15	– / *2.230*	– / *2.097*	– / *2.223*	2.220(4) / *2.24*	2.249(2)
M2–C16	– / *2.155*	– / *2.022*	– / *2.168*	2.174(5) / *2.17*	2.180(2)
M2–C17	– / *2.156*	– / *2.022*	– / *2.168*	2.191(4) / *2.17*	2.193(2)
M2–C18	– / *2.225*	– / *2.097*	– / *2.225*	2.220(4) / *2.25*	2.252(2)
M2–C19	– / *2.655*	– / *2.464*	– / *2.611*	2.434(4) / *2.64*	2.317(2)
M2–C20	– /*2.649*	– / *2.464*	– / *2.609*	2.436(4) / *2.64*	2.336(2)
M1–C(Cp) (av.)	–	–	–	2.179(5) / *2.20*	2.205(27)
C11–C12	1.414(1) / *1.435*	1.431(4) / *1.431*	– / *1.431*	1.427(7) / *1.44*	1.450(2)
C12–C13	1.412(1) / *1.421*	1.406(4) / *1.420*	– / *1.420*	1.395(6) / *1.42*	1.407(3)
C13–C14	1.448(1) / *1.436*	1.420(4) / *1.431*	– / *1.431*	1.440(6) / *1.43*	1.442(2)
C15–C16	– / *1.441*	– / *1.433*	– / *1.438*	1.418(6) / *1.44*	1.421(3)
C16–C17	– / *1.421*	– / *1.420*	– / *1.422*	1.398(6) / *1.42*	1.409(3)
C17–C18	– / *1.440*	– / *1.433*	– / *1.438*	1.418(7) / *1.44*	1.423(3)
C14–C20	1.422(1)	1.428(1)	–	1.440(6) / *1.44*	1.454(2)
C20–C15	1.442(1)	1.435(1)	–	1.427(6) / *1.44*	1.413(2)
C12–C19	–	–	–	1.417(6) / *1.44*	1.416(2)
C19–C11	–	–	–	1.457(6) / *1.44*	1.460(3)
Fold angles	14.6(1)[c] / *12.96*	12.4(2)[c] / *11.77*	–, – / *11.97, 15.93*	25.2(4)[c], 8.6(4)[d] / *11.2, 7.8*	31.5(1)[e]

[a] Values taken from ref. 11c. [b] Values taken from ref. 7d. [c] Dihedral angle C11–C12–C13–C14 / C14–C20–C19–C11. [d] Dihedral angle C15–C16–C17–C18 / C18–C19–C20–C15. [e] Dihedral angle C11–C12–C13–C14 / C14–C20–C15–C16–C17–C18–C19–C11.

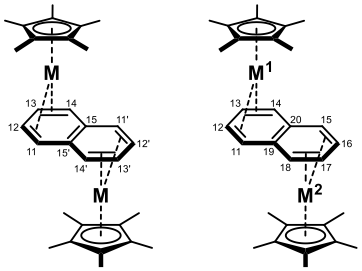

Figure 6 Numbering scheme for naphthalene bridged complexes.

NMR Spectroscopic Characterization

In accord with the symmetric structure observed for **1** in the solid state, the ^{1}H NMR spectrum in C_6D_6 shows a single Cp* resonance at 1.84 ppm and two multiplets at 4.89 and 2.17 ppm, which are assigned to the hydrogen atoms of the naphthalene ligand. The naphthalene signals are notably shifted to lower frequency relative to free naphthalene. An even more pronounced chemical shift difference is observed for the related Cp*-substituted diiron and iron-ruthenium complexes **J** and **T** (Table 2), which display strongly shielded 1,4-hydrogen signals (1.11 ppm for **J**, 1.31 ppm for **T**). The diruthenium complex **1** shows a less pronounced low frequency shift for the 1,4-hydrogen atoms (H11 and H14) than **J** and **T**, but the 2,3-hydrogen atoms (H12 and H13) are somewhat more shielded. The same trend is observed in the ^{13}C{^{1}H} NMR spectra of **1**, **J**, and **T**. In all cases, the 1,4-carbon signals are shifted to higher field, as are the 2,3-carbon signals. While the difference to the spectrum of free naphthalene is striking, the ^{13}C{^{1}H} NMR spectra of **1**, **J**, and **T** show only marginally different chemical shifts for the naphthalene carbon atoms.

It is interesting to compare the ^{1}H NMR data of **1** with those of the related *syn*-facial complex **Q**. In C_6D_6 solution, **Q** is fluxional and thus gives a symmetric ^{1}H NMR spectrum. Resonances for

Dalton Transactions

ARTICLE

Table 2 Assignment of ^{1}H and $^{13}C\{^{1}H\}$ NMR resonances of **1**, **J**, **T**, **Q** and free naphthalene. $^{13}C\{^{1}H\}$ resonances are given in parentheses. See Figure 6 for the numbering scheme.

	1	**J**	**T**	**Q**	Free $C_{10}H_8$
$H_{11,14,15,18}$ ($C_{11,14,15,18}$)	2.17 (60.9)	1.11 (58.0)	1.31, 1.80 (58.8, 59.5)	3.71 (–)	7.63 (128.2)
$H_{12,13,16,17}$ ($C_{12,13,16,17}$)	4.89 (72.5)	5.72 (77.5)	5.10, 5.27 (72.0, 76.4)	4.88 (–)	7.24 (126.1)
$C_{19,20}$	(not obs.)	(110.1)	(110.8)	–	(134.0)
CH_3 of Cp*	1.84 (11.6)	1.49 (10.1)	1.64, 1.77 (10.3, 11.5)	–	
Quat. C of Cp*	(85.8)	(83.8)	(82.6, 85.1)	–	

the naphthalene ligand of **Q** were observed at 3.71 and 4.88 ppm.[7d]

Cyclic Voltammetry and UV-vis Spectroelectrochemistry

In order to gain insight into the redox properties of **1**, we recorded a cyclic voltammogram in THF/TBAH (Figure 7). The reduction potentials and peak-to-peak separations are summarized in Table 3 along with data for some related compounds. The CV of **1** shows two well-separated oxidation processes **1** → $\mathbf{1}^{+}$ (–1.47 V vs. Fc/Fc^{+}) and $\mathbf{1}^{+}$ → $\mathbf{1}^{2+}$ (–1.25 V vs. Fc/Fc^{+}), which are fully reversible under the experimental conditions. The cyclic voltammograms of the analogous diiron and iron-ruthenium complexes **J** and **T** and the *syn*-facial dicyclopentadiene complex **Q** are qualitatively similar. Notably, the separation of the half-wave potentials $\Delta E_{1/2}$ = 220 mV is similar for **Q** (180 mV), but substantially larger for **J** (660 mV) and **T** (590 mV). While **J** and **T** show a quasireversible reduction

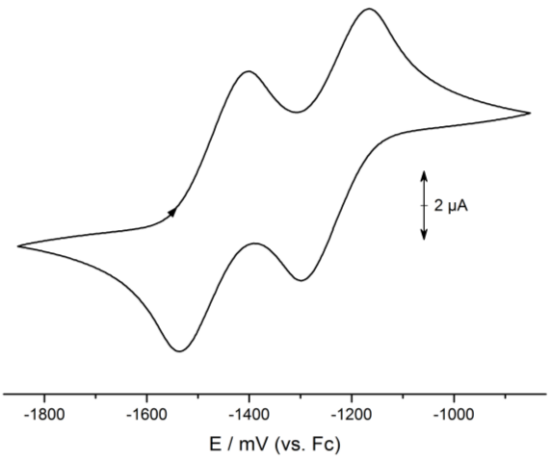

Figure 7. Cyclic voltammogram of **1**, recorded in THF / NBu_4PF_6 at v = 100 mV s^{-1}. Working electrode: Pt minidisk, counter electrode: Pt wire, pseudoreference electrode: Ag wire.

around –3.0 to –3.1 V,[11] no such reduction wave was observed for **1**. The anthracene-bridged complex $\mathbf{F}^{2+}$ (Figure 1) displays two reductions at $E_{1/2}$ = –0.78 and –1.47 V with a separation of 690 mV, while related complexes $[Cp^*Ru(\mu\text{-}L)RuCp^*]^{2+}$ ($\mathbf{L}^{2+}$-$\mathbf{O}^{2+}$) with non-linear polyarenes (phenanthrene, pyrene and chrysene) feature two redox processes at substantially more negative potentials than **1** ($\Delta E_{1/2}$ = 130 to 690 mV). From these data, it appears that the nature of the bridging ligand has a more profound influence on the redox potential than the metal atom or the cyclopentadienyl ligand.

Table 3 Redox potentials ($E_{1/2}$ vs. Fc/Fc^{+} in V) and ΔE_P (in V) of some dinuclear polyarene-bridged complexes determined by cyclic voltammetry (THF / NBu_4PF_6, Pt disk working electrode unless noted otherwise); see Figures 1-3 for the molecular structures.

	$[M] \leftrightarrows [M]^{+}$	ΔE_P	$[M]^{+} \leftrightarrows [M]^{2+}$	ΔE_P	$\Delta E_{1/2}$
1	–1.47	0.11	–1.25	0.10	0.22
J	–1.61	0.09	–0.95	0.09	0.66
T	–1.64	–	–1.05	–	0.59
Q [d]	–1.32	–	–1.14	–	0.18
$\mathbf{L}^{2+}$ [a]	–1.47	0.08	–0.78	0.09	0.69
$\mathbf{M}^{2+}$ [a]	–1.96	0.15	–1.78	0.10	0.18
$\mathbf{N}^{2+}$ [a]	–1.91	0.08	–1.68	0.07	0.13
$\mathbf{O}^{2+}$ [b]	–2.07	0.21	–1.75[c]	0.06	–

[a] Ref. 7a. [b] Ref. 7b. [c] E_{Pc} values instead of $E_{1/2}$. [d] measured in acetonitrile / NBu_4PF_6; ΔE_P not available.

The changes in the electronic transitions upon oxidation of $\mathbf{1}^{0}$ to $\mathbf{1}^{+}$ and $\mathbf{1}^{2+}$ were monitored by UV-vis spectroelectrochemistry using an OTTLE cell.[15] While both oxidation steps were found to be fully reversible at a scan rate of v = 100 mV s^{-1}, i.e. on a time scale of 20 s, the neutral species $\mathbf{1}^{0}$ could be only partially recovered after a CV measurement at v = 2 mV s^{-1} (74% of original amount). When performing the oxidation and back-reduction in rapid potential steps rather than a slow CV, 85% of the starting material were recovered.

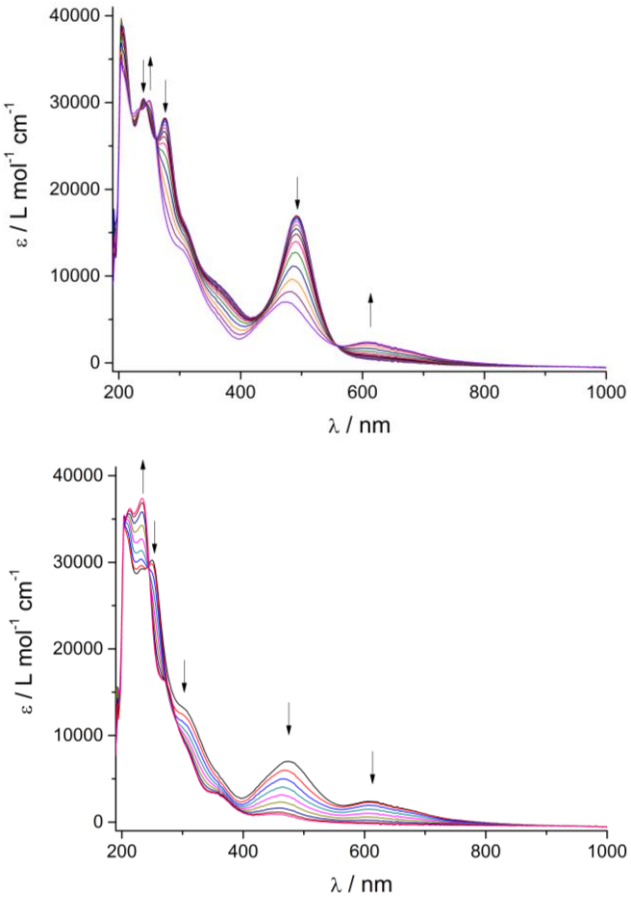

Figure 8 UV-vis spectral changes accompanying the electrochemical oxidations **1** → **1**$^{+}$ (top) and **1**$^{+}$ → **1**$^{2+}$ (bottom) on a Pt minigrid in THF / NBu_4PF_6 (v = 2 mV s^{-1}).

The UV-vis spectrum of **1** shows a band in the visible region at 492 nm and UV bands at 309, 274, 240 and a shoulder at 370 nm. Upon oxidation to **1**$^{+}$ (Figure 8, top), these bands disappear and a new broad and weak band arises at 609 nm with a shoulder at 680 nm. Two additional bands at 467 and 250 nm become visible. When **1**$^{+}$ is oxidized further to **1**$^{2+}$ (Figure 8, bottom), the bands in the visible range disappear and the original UV bands of **1** appear along with a new, relatively weak band at 365 nm. Upon back reduction, the spectra of **1**$^{+}$ and subsequently of **1** are recovered.

Comparing the UV-vis spectra of **J**, **T** and **1**, it is evident that replacing iron by ruthenium leads to a shift of the main visible band to higher energy, from 675 nm for **J**[11b] to 599 nm for **T**[11c] to 492 nm for **1**. Complex **Q** gives rise to a similar UV-vis spectrum with a maximum at 454 nm and a shoulder around 600 nm. Notably, Chin and co-workers reported that the visible bands are associated with similar transitions as those giving rise to the visible band of **1** (*vide infra*).[7d] In all four complexes, oxidation to the mixed-valence species leads to the appearance of a new, very broad and weak band at lower energy (around 900 nm for **J**$^{+}$, 796 nm for **T**$^{+}$, 854 nm for **Q**$^{+}$, 609 nm and 680sh for **1**$^{+}$). In **J**$^{+}$, **T**$^{+}$ and **1**$^{+}$, another band appears at slightly higher energy relative to the visible absorption of the neutral complex (633 nm for **J**$^{+}$, 591 nm for **T**$^{+}$ and 467 nm for **1**$^{+}$). The oxidation to the dications **J**$^{2+}$, **T**$^{2+}$, and **1**$^{2+}$ leads to the disappearance of all bands in the visible region.

Quantum chemical calculations

In order to gain more insight into the properties of **1**, we performed DFT calculations at the BP86/def2-TZVP level of theory.[16,17] A geometry optimization without symmetry constraints gave a nearly C_{2h} symmetrical structure in close agreement with the structure determined by X-ray crystallography (Table 1), with the difference in bond lengths remaining below 0.07 Å. An analysis of the frontier molecular orbitals (Figure 9) shows that the HOMO is largely metal-centered with smaller contributions from the naphthalene and Cp* ligands, while the lower lying orbitals (HOMO-1 and HOMO-2) are essentially composed of d orbitals of the two ruthenium centers. HOMO-3 and HOMO-4 are largely associated with one metal center each with small ligand contributions. By contrast, the LUMO displays larger contributions from the naphthalene

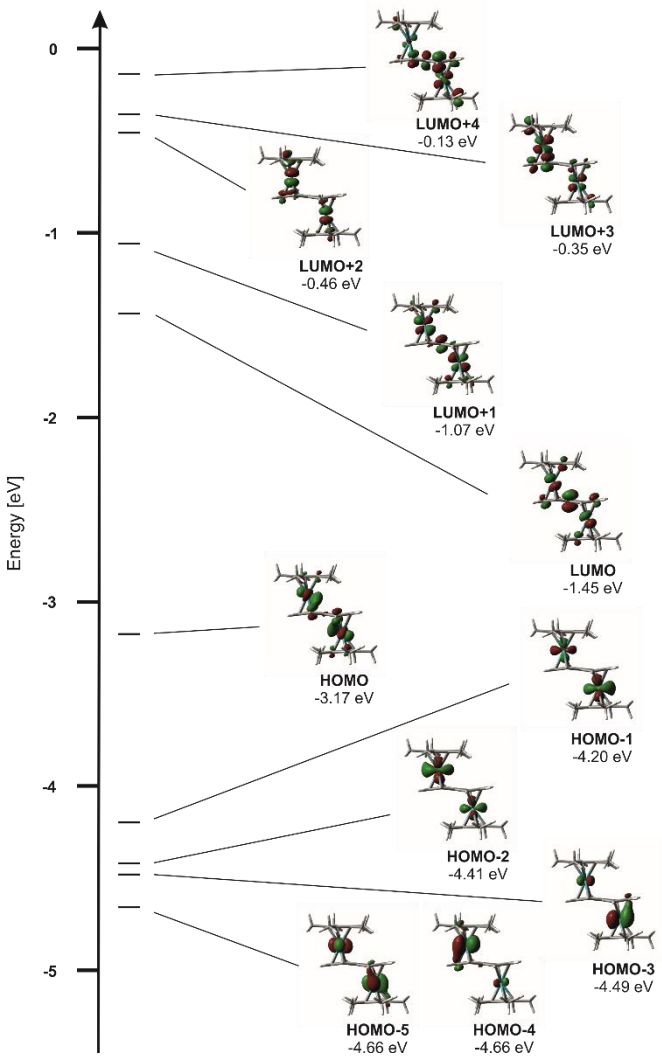

Figure 9 Frontier molecular orbitals of **1**, calculated with DFT at the BP86/def2-TZVP level of theory (molecular orbitals generated with GaussView 5.0).

ligand, as do the higher lying orbitals LUMO+1, LUMO+3 and LUMO+4. The LUMO+2 shows interactions of metal d orbitals and the Cp* ligands with only minor contributions from the naphthalene ligand. Comparison with the diiron complex **J** and the iron-ruthenium complex **T** shows that the composition of the molecular orbitals is largely identical in the three complexes.

The experimental UV-vis spectrum of **1** is reproduced well by TD-DFT calculations at the B3LYP/def2-TZVP level (see the ESI for details). The only band in the visible region at 492 nm is composed of transitions from the HOMO-2 to the LUMO as well as from the HOMO to the LUMO+1. The band observed at 309 nm appears to be of complex origin, involving excitations from several occupied MOs (HOMO-1, HOMO-2 and HOMO-4) to diverse unoccupied MOs (LUMO, LUMO+1 and LUMO+3).

Chemical Oxidation of [Cp*Ru(μ-$C_{10}H_8$)RuCp*] (1)

Generation of Hydride Complexes. Since the electrochemical measurements indicated that the monocationic species $\mathbf{1}^+$ is stable, we attempted to synthesize it on a preparative scale. However, attempted oxidations of **1** with ferrocenium hexafluorophosphate in THF did not yield $\mathbf{1}^+$. Instead, the cationic hydride complex [**3**]PF_6 was identified as one of the products by ^{1}H NMR spectroscopy and X-ray crystallography, presumably due to traces of residual moisture. This is in contrast to reactions of **J** and **T**, which cleanly afforded the one-electron oxidation products $\mathbf{J}^+$ and $\mathbf{T}^+$.[11c,12]

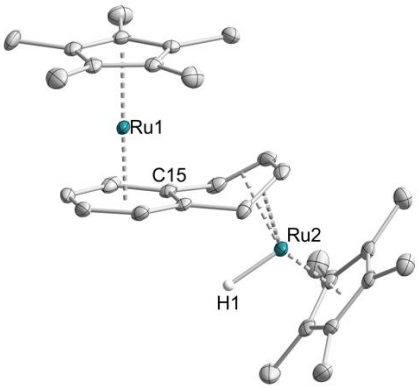

Figure 10. Solid-state X-ray structure of $\mathbf{[3]}^+$ (thermal ellipsoids at 50% probability; hydrogen atoms except H1 and PF_6^- anion omitted for clarity).

Single crystals of [**3**]PF_6 suitable for X-ray diffraction were grown by layering a THF solution of the compound with *n*-hexane and storage at –30°C. [**3**]PF_6 crystallizes in the triclinic space group *P*–1 with two molecules and one equivalent of THF in the unit cell. The molecular structure of $\mathbf{[3]}^+$ (Figure 10) features two distinct Ru centers. While one ruthenium atom is coordinated by the naphthalene ligand in an η^6 fashion, the other ruthenium center is η^4-coordinated by naphthalene and bound by the hydride ligand, resulting in a 36 electron complex with both Ru centers in a formal oxidation state of +II. The asymmetric coordination of the naphthalene results in a significant folding along the C15/18 vector by 36.5(1)°, which is in line with analogous η^4-naphthalene complexes (*vide supra*).

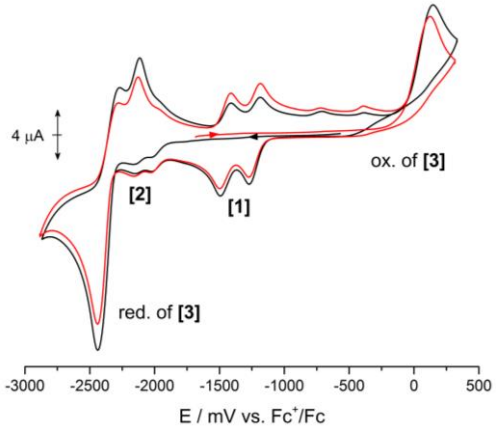

Figure 11. Cyclic voltammogram of [**3**]BAr^F_4, recorded in THF / NBu_4PF_6 at v = 100 mV s^{-1}. Working electrode: Pt minidisk, counter electrode: Pt wire, pseudoreference electrode: Ag wire.

To investigate $\mathbf{3}^+$ in more detail, we developed a rational

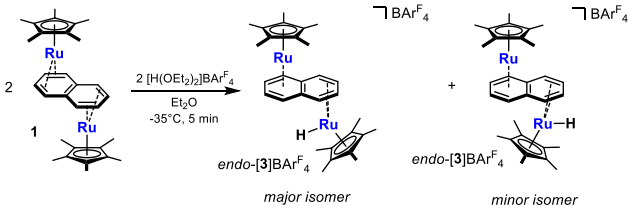

Scheme 2. Preparation of [**3**]BAr^F_4 from **1** and Brookhart's acid, $[H(OEt_2)_2]BAr^F_4$.

synthesis by protonation of **1** with Brookhart's acid, $[H(OEt_2)_2]BAr^F_4$[18] in diethyl ether (Scheme 2). After layering a concentrated diethyl ether solution with *n*-hexane, [**3**]BAr^F_4 was obtained as a colourless crystalline solid in 56% yield. The diamagnetic complex gives rise to sharp signals in the ^{1}H NMR spectrum (recorded in C_6D_6). As observed for **1**, the naphthalene ligand signals shifted to higher field with respect to free naphthalene. to 2.82 , 3.78, 4.86 and 4.14 ppm. The hydride signal is found at –2.95 ppm. The two Cp* rings give rise to signals at 1.41 and 1.17 ppm, while the $BAr^F_4{}^-$ protons resonate at 8.42 and 7.72 ppm. It is noteworthy that a second set of signals can be observed when recording the spectrum immediately after adding $[H(OEt_2)_2]BAr^F_4$ to **1** in THF-d_8. The ^{1}H NMR resonances of this second species are shifted slightly upfield relative to the major product with a hydride resonance at –3.09 ppm and signals for the naphthalene ligand at 2.68, 3.75, 4.04 and 4.69 ppm, respectively. Only the major product is observed after storing the NMR sample overnight. Presumably, the minor species is an isomer of [**3**]BAr^F_4 where the hydride atom points away from the naphthalene ligand ("*exo*-hydride", Scheme 2).

Our DFT calculations revealed that the main isomer ("*endo*-hydride" *endo*-[**3**]BAr^F_4) is more stable than the *exo*-isomer *exo*-[**3**]BAr^F_4 by 39.5 kJ mol^{-1} at the BP86/def2-TZVP level. Since the attack of the proton should proceed from the sterically least hindered position, the *exo*-hydride is assumed to be the kinetically favoured species which slowly converts to the thermodynamically more stable *endo*-hydride complex.

Dalton Transactions

ARTICLE

Table 4 Structural parameters of $\mathbf{1}^+$, $\mathbf{J}^+$, $\mathbf{S}^+$ and $\mathbf{T}^+$ obtained by X-ray crystallography and DFT calculations. DFT values given in italics. Numbering according to Figure 6.

	$\mathbf{1}^+$ (M^1 = M^2 = Ru)	$\mathbf{J}^+$[a] (M^1 = M^2 = Fe)	$\mathbf{S}^+$[b] (M^1 = Fe, M^2 = Ru)	$\mathbf{T}^+$[c] (M^1 = Fe, M^2 = Ru)
M1–C11	2.220(3) / *2.223*	2.083(2) / *2.099*	– / *2.11*	2.100(3) / *2.12*
M1–C12	2.192(3) / *2.195*	2.052(3) / *2.063*	– / *2.00*	2.027(3) / *2.04*
M1–C13	2.200(3) / *2.196*	2.052(2) / *2.063*	– / *2.00*	2.030(3) / *2.04*
M1–C14	2.230(3) / *2.223*	2.084(2) / *2.099*	– / *2.11*	2.082(3) / *2.12*
M1–C19	2.416(3) / *2.425*	2.256(3) / *2.359*	– / *2.46*	2.690(3) / *2.63*
M1–C20	2.418(3) / *2.425*	2.253(3) / *2.359*	– / *2.46*	2.677(3) / *2.63*
M1–C(Cp) (av.)	2.183(2)	–	– / *2.10*	2.119(3) / *2.12*
M2–C15	–	–	– / *2.25*	2.227(3) / *2.24*
M2–C16	–	–	– / *2.16*	2.210(3) / *2.21*
M2–C17	–	–	– / *2.16*	2.211(3) / *2.21*
M2–C18	–	–	– / *2.25*	2.222(3) / *2.24*
M2–C19	–	–	– / *2.74*	2.277(3) / *2.38*
M2–C20	–	–	– / *2.74*	2.269(3) / *2.38*
M2–C(Cp) (av.)	–	–	– / *2.20*	2.178(3) / *2.20*
C11–C12	1.404(5) / *1.425*	1.403(4) / *1.430*	– / *1.43*	1.415(5) / *1.43*
C12–C13	1.417(6) / *1.423*	1.408(4) / *1.425*	– / *1.42*	1.396(5) / *1.42*
C13–C14	1.416(5) / *1.425*	1.414(4) / *1.430*	– / *1.43*	1.416(5) / *1.43*
C15–C16	–	–	– / *1.44*	1.412(5) / *1.42*
C16–C17	–	–	– / *1.43*	1.414(5) / *1.42*
C17–C18	–	–	– / *1.44*	1.415(5) / *1.42*
C14–C20	1.430(5)	1.428(4) / *1.445*	– / *1.43*	1.470(4) / *1.46*
C20–C15	–	–	– / *1.44*	1.422(5) / *1.43*
C18–C19	–	–	– / *1.44*	1.418(4) / *1.43*
C19–C11	1.437(5)	1.442(4) / *1.445*	– / *1.43*	1.469(5) / *1.46*
Fold angles	7.9(2)[d] / *8.35*	6.6(2)[d]	–, – / *13.9*[d], *21.1*[e]	28.7[d], 1.7[e] / *12.4*[d], *2.4*[e]

[a] X-ray and DFT values taken from ref. 12. [b] DFT values taken from ref. 11c. [c] X-ray and DFT values taken from ref. 11c. [d] Dihedral angle C11–C12–C13–C14 / C14–C20–C19–C11. [e] Dihedral angle C15–C16–C17–C18 / C18–C19–C20–C15.

The electrochemical analysis of [**3**]BAr^F_4 showed an irreversible oxidation at E_{Pa} = –0.13 V as well as a strong, quasireversible reduction at –2.36 V (Figure 11). Notably, complex **1** is reformed upon both of these irreversible processes along with a minor amount of the mononuclear cation $\mathbf{2}^+$. The absence of redox waves corresponding to **1** at the start of the measurement confirms that **1** (or $\mathbf{1}^{2+}$) is only formed upon electrochemical reduction or oxidation, respectively.

Preparation of [Cp*Ru(μ-$C_{10}H_8$)RuCp*]$^+$ ($\mathbf{1}^+$). The desired monooxidation product $\mathbf{1}^+$ can be obtained using $[Cp_2Fe]BAr^F_4$ instead of $[Cp_2Fe]PF_6$ as the oxidizing agent and diethyl ether rather than THF as the solvent. After removing the by-product ferrocene and recrystallizing from diethyl ether, [**1**]BAr^F_4 was obtained in excellent yield as an olive-green crystalline solid. X-ray quality crystals were grown by slow evaporation of the solvent from a concentrated diethyl ether solution of [**1**]BAr^F_4. The molecular structure of [**1**]BAr^F_4 (Figure 12), which

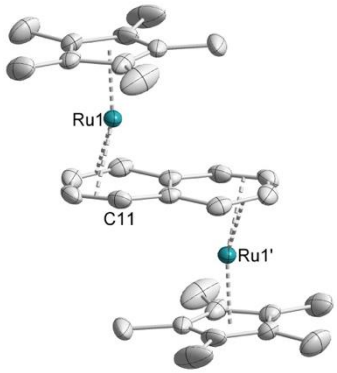

Figure 12. Solid-state X-ray structure of $[\mathbf{1}]^+$ (thermal ellipsoids at 50% probability; hydrogen atoms and Bar^F_4 counterion omitted for clarity).

crystallizes in the triclinic space group *P*–1, shows contracted Ru1–C15 and Ru1–C15' distances relative to those in complex **1** by 0.17 Å, which indicate that the hapticity of the naphthalene is between η^4 and η^6 in this case. This change and the smaller fold angle of 7.9° are consistent with less electron-rich metal centers and a smaller degree of back-bonding. Structural parameters obtained by DFT calculations at the BP86/def2-TZVP level of theory are in very good agreement with the values from X-ray crystallography. A list of relevant structural parameters is given in Table 4.

Due to the paramagnetic nature of **1**$^+$, no signals were observed in the ^{1}H NMR spectrum. The magnetic moment was determined by the Evans method. The observed value of μ_{eff} = 1.3(1) μ_B is lower than the expected spin-only value of 1.73 μ_B for a complex featuring one unpaired electron. The EPR spectrum of [**1**]BAr$^F_4$ reveals the presence of two species (Figure 13). The main species, representing ~97% of the total signal intensity, apparently corresponds to **1**$^+$. The species reveals a rhombic spectrum with (poorly resolved) Ru hyperfine interactions (HFIs) along the g_y value (Figure 13, Table 5). The HFI seem to stem from a single ruthenium nucleus (coupling to ^{99}Ru and ^{101}Ru, ~40 MHz, I = 5/2, 30% natural abundance). The minor species, representing only 3% of the total signal intensity, reveals an isotropic signal with g-values around 2.008. While the nearly isotropic nature of the signal may suggest the presence of an organic radical, the g-value perhaps deviates a bit too much from g_e to correspond to a pure organic radical like the naphthalene radical anion. As such, this minor signal probably stems from a second metal complex of unknown structure. Repeated experiments of several different samples of [**1**]BAr$^F_4$ in all cases revealed the presence of both components in similar ratios.

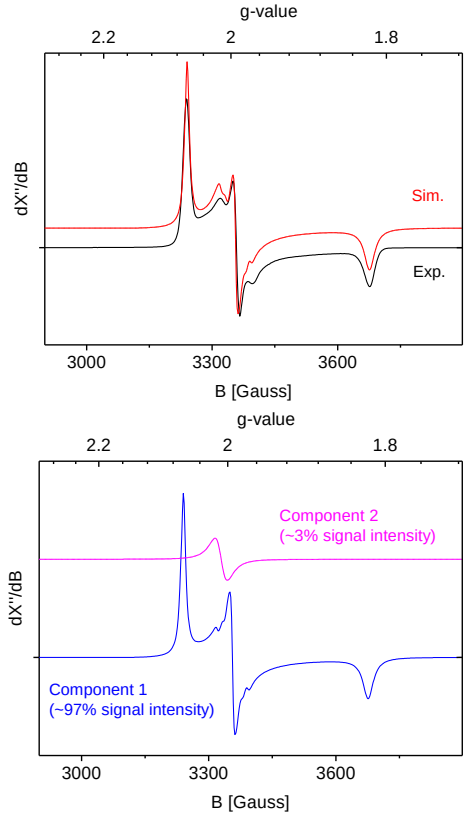

Figure 13 Top: experimental and simulated EPR spectra of **1**$^+$ measured in frozen THF at 20 K (NBu_4PF_6 added to obtain a better glass). Experimental parameters: Microwave frequency 9.363205 GHz, microwave power 0.632 mW, modulation amplitude 4 G. Simulation was obtained with the parameters shown in Table 5, assuming contributions of two species (bottom).

Table 5 Parameters used in the EPR simulations.

	Component 1	Component 2
g-tensor		
g_x	1.819	2.008
g_y	1.992	2.008
g_z	2.063	2.008
Hyperfine interactions (MHz)		
A^{Ru}_x	NR	–
A^{Ru}_y	40	–
A^{Ru}_z	NR	–

The UV-vis spectrum of [**1**]BAr$^F_4$ (recorded in diethyl ether) is identical with the spectrum recorded by UV-vis spectroelectrochemistry (*vide supra*), showing a relatively strong band 469 nm and a weaker absorption 609 nm with a shoulder at 680 nm. The degree of electronic interaction between the two metal centers in a dinuclear complex can be estimated utilizing the theories of Hush, Brunschwig, Creutz and Sutin, by analyzing the ratio of the theoretical half-height width of the intervalence transition band with the observed line width.[19] Unfortunately, a reliable analysis using Hush theory was not possible for [**1**]BAr$^F_4$ due to the severe overlap of the absorption bands at 609 and 680sh nm. Therefore, we investigated the electronic structure of **1**$^+$ (the cation in [**1**]BAr$^F_4$) by DFT calculations. The def2-TZVP basis set and various pure and hybrid functionals were used (BP86, B3LYP, CAM-B3LYP and BLYP35).[20] The frontier molecular orbitals are qualitatively similar to **1** with these functionals (see Figure S8 in the ESI). The SOMO shows a high degree of symmetry with equal contributions from both metal centers. The spin density (Figure 14) is largely centered on the metal centers with minor contributions from the naphthalene and Cp* ligands. The contribution of both Ru centers is the same. These calculations support the assignment of **1**$^+$ as a fully charge-delocalized class III species.[21] However, it should be noted that making a distinction between class III and borderline class II species is intricate even when several complementary spectroscopic techniques are applied.[22]

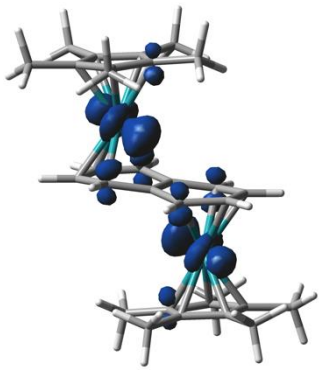

Figure 14. Spin density distribution of **1**$^+$ calculated at the BP86/def2-TZVP level of theory (spin density plot generated using GaussView 5.0).

Conclusions

We report a series of new diruthenium compounds [Cp*Ru(μ-$C_{10}H_8$)RuCp*] (**1**), [Cp*Ru(μ-$C_{10}H_8$)RuCp*]$BAr^F{}_4$ [**1**]$BAr^F{}_4$ and [Cp*Ru(μ-$\eta^{6:}\eta^4$-$C_{10}H_8$)Ru(H)Cp*]$BAr^F{}_4$ ([**3**]$BAr^F{}_4$), which complement the existing literature on related diiron, iron-ruthenium and diruthenium complexes. Diruthenium complex **1** is readily prepared by the reduction of the well-known ruthenium(II) precursor [Cp*Ru($C_{10}H_8$)]PF_6 ([**2**]PF_6) with KC_8, while [**1**]$BAr^F{}_4$ and [**3**]$BAr^F{}_4$ are accessible from **1** by oxidation and protonation, respectively. All three complexes were isolated in moderate yields and were fully characterized by X-ray crystallography, spectroscopic techniques, cyclic voltammetry and UV-vis spectroelectrochemistry and DFT calculations. The structures are similar to recently reported complexes [Cp^RFe(μ-$C_{10}H_8$)MCp*] (Cp^R = C_5Me_5, 1,2,4-$C_5H_2tBu_3$; M = Fe (**H-K**), Ru (**S-T**). However, related diruthenium complexes are still scarce. The few known examples (Figure 2) were only partially characterized or display different structural arrangements due to the presence of dicyclopentadienyl ligands. The complexes presented herein thus provide valuable new data on this class of compounds. In particular, the tendency of the naphthalene bridge to mediate strong electronic coupling between the metal centers is striking. An extension to a wider range of polyarene ligands seems warranted to study this phenomenon in more detail. In addition, the reactivity of hydride complex [**3**]$BAr^F{}_4$ toward oxidation and reduction should also be the subject of future studies.

Experimental Details

General considerations. All reactions were carried out under an inert atmosphere of purified argon using standard Schlenk and glovebox techniques. Solvents were dried by distillation over sodium/benzophenone (DME) or using an MBraun SPS-800 solvent purification system (toluene, *n*-hexane, THF). C_5Me_5H and KC_8 were prepared following standard procedures.[23] Naphthalene was obtained commercially and used as received. ^{1}H and ^{13}C{^{1}H} NMR spectra were recorded with a Bruker Avance 300 spectrometer (300.13 and 75.47 MHz, respectively). ^{1}H and ^{13}C{^{1}H} NMR signals were referenced internally to residual solvent signals. UV-vis spectra were recorded with a Varian Cary 50 spectrometer. Elemental analyses were determined by the analytical department at the University of Regensburg.

Synthesis. [Cp*Ru($C_{10}H_8$)]PF_6 ([**2**]PF_6): [**2**]PF_6 was synthesized following a modified procedure by Williams et. al.[24] A solution of $RuCl_3 \cdot 3\ H_2O$ (1.500 g, 5.640 mmol, 1.0 equiv.) in 50 mL degassed ethanol was slowly added to a solution of naphthalene (3.589 g, 28.00 mmol, 5.0 equiv.) and C_5Me_5H (3.814 g, 28.00 mmol, 5.0 equiv.) in 50 mL ethanol via a dropping funnel. The mixture was refluxed overnight, yielding a dark orange solution. After removing the solvent *in vacuo*, the residue was extracted with 150 mL H_2O and 150 mL diethyl ether. The aqueous phase was washed with 3 × 50 mL diethyl ether. A saturated solution of NH_4PF_6 was added to the aqueous phase to precipitate the complex as an orange solid, which was separated by filtration and washed with diethyl ether. The crude product was dissolved in acetone, filtered over a short alumina column, and subsequently recrystallized from acetone/ethyl acetate, yielding a light yellow crystalline powder. Yield 2.0258 g (71%). ^{1}H NMR (300.13 MHz, $CDCl_3$): δ = 1.64 (s, 15H, Cp*), 5.92 (m, 2H), 6.38 (m, 2H), 7.49 (m, 2H), 7.68 (m, 2H) ppm. ^{13}C{^{1}H} NMR (75.47 MHz, $CDCl_3$): δ = 11.6 (*C*H_3 of Cp*), 60.9 (C11/C14 of coordinated naphthalene), 72.5 (C12/C13 of coordinated naphthalene), 85.8 (C15 of coordinated naphthalene) ppm.

[Cp*Ru(μ-$C_{10}H_8$)RuCp*] (1). [**2**]PF_6 (1.500 g, 2.944 mmol) was suspended in 100 mL DME and cooled to –30 °C. KC_8 (438 mg, 3.239 mmol, 1.1 equiv.) was added, and the mixture was stirred overnight in the cooling bath which slowly warmed to room temperature. The resulting red suspension was filtered over a glass frit. The solvent was removed *in vacuo*, and the residue was extracted with toluene (2 × 15 mL). The deep red solution was concentrated to about 20 mL and cooled to –30 °C, whereupon dichroic red green crystals of **1** formed. Yield: 251 mg (28%). ^{1}H NMR (300.13 MHz, C_6D_6): δ (ppm) = 1.85 (s, 30H, Cp*), 2.17 (m, 4H), 4.89 (m, 4H). ^{13}C{^{1}H} NMR (75.47 MHz, C_6D_6): δ (ppm) = 11.6 (CH_3 of Cp*), 60.9, 72.5, 85.8. UV-vis (THF): λ_{max} / nm (ε_{max} / $dm^3mol^{-1}cm^{-1}$) = 240 (25600), 273 (20800), 309 (11400), 360 (shoulder), 492 (18086). Elemental analysis: $C_{30}H_{38}Ru_2$ (600.77): calcd. C 59.98, H 6.38; found C 59.90, H 6.45. Melting point: 274-280 °C (decomposition to a dark solid and free naphthalene).

[Cp*Ru(μ-$C_{10}H_8$)RuCp*]$BAr^F{}_4$ ([**1**]$BAr^F{}_4$). **1** (60 mg, 0.10 mmol) was dissolved in 15 mL of Et_2O and [Cp_2Fe]$BAr^F{}_4$ (104.8 mg, 0.10 mmol) was added in one portion. A color change from deep red to olive green was observed within seconds. The solvent was removed in vacuo and the residue was washed with n-hexane (3 x 5 mL). The remaining solid was extracted with Et_2O, filtered and dried in vacuo. Yield: 131.6 mg (90%). UV-vis (Et_2O): λ_{max} / nm (ε_{max} / $dm^3mol^{-1}cm^{-1}$) = 469 (6185), 609 (2788), 680 (sh). μ_{eff}(Evans method, THF-d_8, 300 K) = 1.3(1) μ_B. Elemental analysis: $C_{62}H_{50}BF_{24}Ru_2$ (1463.99): calcd. C 50.87, H 3.44; found C 51.38, H 3.71.

[Cp*Ru(μ-$C_{10}H_8$)Ru(H)Cp*]$BAr^F{}_4$ ([**3**]$BAr^F{}_4$). **1** (26.3 mg, 0.043 mmol, 1 equiv.) was dissolved in 10 mL of Et_2O and cooled to -35°C. A solution of [$H(OEt_2)_2$]$BAr^F{}_4$ (88.0 mg, 0.087 mmol, 2

equiv.) in 10 mL of Et_2O was added dropwise, leading to a color change from dark red to light yellow. The solution was concentrated to 10 mL, layered with 20 mL of *n*-hexane and stored at –30°C overnight. The crystalline product was isolated by filtration and dried in vacuo. Yield: 59.1 mg (94%). ^{1}H NMR (300.13 MHz, C_6D_6): **major isomer** (*endo*-[**3**]BAr^F_4) δ (ppm) = –2.93 (s, 1H, hydride), 1.18 (s, 15H, Cp* at Ru1), 1.42 (s, 15H, Cp* at Ru2), 2.83 (m, 2H, H15/18 of coordinated naphthalene), 3.80 (m, 2H, coordinated naphthalene), 4.15 (m, 2H, coordinated naphthalene), 4.86 (m, 2H, H16/17 of coordinated naphthalene), 7.72 (s, 4H, H_{para} of BAr^F_4), 8.41 (s, 8H, H_{ortho} of BAr^F_4); **minor isomer** (*exo*-[**3**]BAr^F_4) δ (ppm) = –3.09 (s, 1H, hydride), 1.07 (s, 15H, Cp* at Ru1), 1.28 (s, 15H, Cp* at Ru2), 2.68 (m, 2H, H15/18 of coordinated naphthalene), 3.75 (m, 2H, coordinated naphthalene), 4.04 (m, 2H, coordinated naphthalene), 4.69 (m, 2H, H16/17 of naphthalene), 7.53 (s, 4H, H_{para} of BAr^F_4), 8.16 (s, 8H, H_{ortho} of BAr^F_4). $^{13}C\{^1H\}$ NMR (75.47 MHz, C_6D_6, only the signals of the major isomer were observed): δ (ppm) = 9.6 ($C_5(CH_3)_5$), 10.2 ($C_5(CH_3)_5$), 48.6 (C15/18 of naphthalene), 79.3 (C16/17 of naphthalene), 79.5 (naphthalene), 80.9 (naphthalene), 118.1 (C_{para} of BAr^F_4), 135.4 (C_{ortho} of BAr^F_4). Elemental analysis: $C_{62}H_{51}BF_{24}Ru_2$ (1465.00): calcd. 50.83, H 3.51; found C 51.11, H 3.51.

X-Ray Crystallography. The crystallographic data for **1,** [**1**]BAr^F and [**3**]PF_6 were collected with an Agilent Technologies SuperNova and an Agilent Technologies Gemini Ultra diffractometer, respectively. The structural data are summarised in Table 4 and crystal data are given in the ESI. The structures wer solved with SHELXT and least-square refinements on F^2 were carried out with SHELXL.[25] The dataset of **1** was twinned. Detwinning was performed using PLATON/TwinRotmat.[26] Only the data for the major component was used for the refinement as the data for the minor component were weak. Details are given in the corresponding CIF files. CCDC 1842108–1842110 contain the supplementary crystallographic data, which can be obtained free of charge from The Cambridge Crystallographic Data Centre via www.ccdc.cam.ac.uk/data_request/cif.

Cyclic Voltammetry. The cyclic voltammogram of **1** was recorded in dry THF in a single-compartment cell connected to a Metrohm Autolab PGSTAT101 potentiostat. The cell was equipped with a Pt disk working electrode polished with 0.25µm diamond paste, a Pt coil auxiliary electrode and an Ag wire pseudoreference electrode. Predried tetrabutylammonium hexafluorophosphate (TBAH) was used as a supporting electrolyte. All redox potentials are reported against the ferrocene/ferrocenium (Fc/Fc^+) redox couple used as an internal standard.

Spectroelectrochemistry. Controlled-potential electrolysis of compound **1** was carried out within an optically transparent thin-layer electrochemical (OTTLE) cell[15] equipped with a Pt minigrid as the working electrode, a Pt coil as the auxiliary electrode and an Ag wire as the pseudoreference electrode, all connected to a Metrohm Autolab PGSTAT302N potentiostat. The UV-vis spectra were recorded using an Agilent Technologies 8453 diode array spectrophotometer. The different redox steps were identified with the aid of the contemporarily recorded thin-layer cyclic voltammogram.

Computational Methods. The calculations on **1**, **1**$^+$ and **3** were performed using the Gaussian09 program package (Revision E.01).[27] The BP86 density functional and the Ahlrichs def2-TZVP basis set were employed for all atoms.[16,17] Atom-pairwise dispersion correction to the DFT energy with Becke-Johnson damping (d3bj) were applied.[28] The nature of stationary point was verified by a numerical frequency analysis. The calculation of the UV-vis spectrum of **1** was performed with the B3LYP hybrid functional and the same TZVP basis set for all atoms.[17,29] Tetrahydrofuran solvent effects were included using the self-consistent reaction field (SCRF), as implemented in Gaussian.[27,30] Molecular orbitals and spin density plots were visualized with GaussView5.[31] The isosurface value is set to 0.05 for all figures.

Conflicts of interest

The authors declare no conflict of interest.

Acknowledgements

The authors thank Dr. M. Bodensteiner (University of Regensburg) for expert crystallographic assistance and Johnson-Matthey for a generous loan of ruthenium trichloride.

Notes and references

†All redox potentials given in this manuscript refer to the Cp_2Fe/Cp_2Fe^+ couple.

‡See the electronic supplementary information for further details.

1. a) D. Astruc, *Acc. Chem. Res.*, 1997, **30**, 383; b) T. Ren, *Organometallics*, 2005, **24**, 4854; c) S. Szafert, J. A. Gladysz, *Chem. Rev.*, 2003, **103**, 4175; d) F. Paul, C. Lapinte, *Coord. Chem. Rev.*, 1998, **178-180**, Part 1, 431.
2. a) A. Ceccon, S. Santi, L. Orian, A. Bisello, *Coord. Chem. Rev.*, 2004, **248**, 683; b) S. Barlow, D. O'Hare, *Chem. Rev.*, 1997, **97**, 637.
3. a) M. N. Bochkarev, I. L. Fedushkin, H. Schumann, J. Loebel, *J. Organomet. Chem.*, 1991, **410**, 321; b) B. F. Bush, J. J. Lagowski, *J. Organomet. Chem.* 1990, **386**, 37; c) S. Sun, C. A. Dullaghan, G. B. Carpenter, A. L. Rieger, P. H. Rieger, D. A. Sweigart, *Angew. Chem. Int. Ed. Engl.*, 1995, **34**, 2540.
4. a) W. H. Morrison, E. Y. Ho, D. N. Hendrickson, *J. Am. Chem. Soc.*, 1974, **96**, 3603; b) W. H. Morrison, E. Y. Ho, D. N. Hendrickson, *Inorg. Chem.*, 1975, **14**, 500.
5. a) A. J. Frings, PhD dissertation, Ruhr-Universität Bochum, Germany, 1988; b) P. Klusmann, PhD dissertation, Ruhr-Universität Bochum, Germany, 1993; c) K. Jonas, *Pure Appl. Chem.* **62**, 1169 (1990).
6. D. S. Perekalin, A. R. Kudinov, *Coord. Chem. Rev.*, 2014, **276**, 153.
7. a) U. Kölle, M. H. Wang, *Organometallics*, 1990, **9**, 195; b) I. Chavez, A. Cisternas, M. Otero, E. Román, U. Müller, *Z.*

Naturforsch., 1990, **45b**, 658; c) I. Chavez, M. Otero, E. Román, U. Müller, *J. Organomet. Chem.*, 1992, **427**, 369; d) H. Salembier, J. Mauldin, T. Hammond, R. Wallace, E. Alqassab, M. B. Hall, L. M. Pérez, Y.-J. A. Chen, K. E. Turner, E. Bockoven, W. Brennessel, R. M. Chin, *Organometallics*, 2012, **31**, 4838; e) for related complexes, see also: P. J. Fagan, M. D. Ward, J. C. Calabrese, *J. Am. Chem. Soc.*, 1989, **111**, 1698.

8. A. Woolf, A. B. Chaplin, J. E. McGrady, M. A. M. Alibadi, N. Rees, S. Draper, F. Murphy, A. S. Weller, *Eur. J. Inorg. Chem.*, 2011, 1614.
9. M. A. Bennett, Z. Lu, X. Wang, M. Bown, D. C. R. Hockless, *J. Am. Chem. Soc.*, 1998, **120**, 10409.
10. a) R. Wolf, C. J. Slootweg, A. W. Ehlers, F. Hartl, B. de Bruin, M. Lutz, A. L. Spek, K. Lammertsma, *Angew. Chem.*, 2009, **121**, 3150; *Angew. Chem. Int. Ed.*, 2009, **48**, 3104; b) R. Wolf, N. Ghavtadze, K. Weber, E.-M. Schnöckelborg, B. de Bruin, A. W. Ehlers, K. Lammertsma, *Dalton Trans.*, 2010, **39**, 1453; c) R. Wolf, E.-M. Schnöckelborg, *Chem. Commun.*, 2010, **46**, 2832; d) E.-M. Schnöckelborg, J. J. Weigand, R. Wolf, *Angew. Chem.*, 2011, **123**, 6787; *Angew. Chem. Int. Ed.*, 2011, **50**, 6657; e) K. Weber, E.-M. Schnöckelborg, R. Wolf, *ChemCatChem*, 2011, **3**, 1572; f) B. Rezaei Rad, D. Herrmann, C. Lescop, R. Wolf, *Dalton Trans.*, 2014, **43**, 4247; g) D. Gärtner, A. Welther, B. Rezaei Rad, R. Wolf, A. Jacobi von Wangelin, *Angew. Chem. Int. Ed.*, 2014, **53**, 3722.
11. a) E.-M. Schnöckelborg, PhD dissertation, University of Münster, Germany, 2011; b) E.-M. Schnöckelborg, F. Hartl, T. Langer, R. Pöttgen, R. Wolf, *Eur. J. Inorg. Chem.*, 2012, 1632; c) J. Malberg, E. Lupton, E.-M. Schnöckelborg, B. de Bruin, J. Sutter, K. Meyer, F. Hartl, R. Wolf, *Organometallics*, 2013, **32**, 6040.
12. T. Hatanaka, Y. Ohki, T. Kamachi, T. Nakayama, K. Yoshizawa, M. Katada, K. Tatsumi, *Chem. Asian J.*, 2012, **7**, 1231.
13. O. V. Gusev, M. A. Ievlev, M. G. Peterleitner, S. M. Peregudova, L. I. Denisovich, P. V. Petrovskii, N. A. Ustynyuk, *J. Organomet. Chem.*, 1997, **534**, 57.
14. E.-M. Schnöckelborg, M. M. Khusniyarov, B. de Bruin, F. Hartl, T. Langer, M. Eul, S. Schulz, R. Pöttgen, R. Wolf, *Inorg. Chem.*, 2012, **51**, 6719.
15. M. Krejčík, M. Daněk, F. Hartl, *J. Electroanal. Chem.*, 1991, **317**, 179.
16. a) C. Lee, W. Yang, R. G. Parr, *Phys. Rev. B: Condens. Matter Mater. Phys.,* 1988, **37**, 785; b) A. D. Becke, *J. Chem. Phys.,* 1993, **98**, 1372.
17. a) A. Schäfer, H. Horn, R. Ahlrichs, *J. Chem. Phys.,* 1992, **97**, 2571; b) F. Weigend, R. Ahlrichs, *Phys. Chem. Chem. Phys.,* 2005, **7**, 3297.
18. M. Brookhart, B. Grant, A. F. Volpe, Jr., *Organometallics*, 1992, **11**, 3920.
19. a) G. C. Allen, N. S. Hush, *Prog. Inorg. Chem.*, 1967, **8**, 357; b) B. S. Brunschwig, C. Creutz, N. Sutin, *Chem. Soc. Rev.*, 2002, **31**, 168.
20. a) M. Renz, K. Theilacker, C. Lambert, M. Kaupp, *J. Am. Chem. Soc.*, 2009, **131**, 16292; b) M. Parthey, J. B. G. Gluyas, P. A. Schauer, D. S. Yufit, J. A. K. Howard, M. Kaupp, P. J. Low, *Chem. Eur. J.,* 2013, **19**, 9780; c) M. Parthey, J. B. G. Gluyas, M. A. Fox, P. J. Low, M. Kaupp, *Chem. Eur. J.,* 2014, **20**, 6895; d) M. Parthey, M. Kaupp, *Chem. Soc. Rev.,* 2014, **43**, 5067; e) M. Kaupp, M. Renz, M. Parthey, M. Stolte, F. Werthner, C. Lambert, *Phys. Chem. Chem. Phys.,* 2011, **13**, 16973.
21. M. B. Robin, P. Day, *Adv. Inorg. Chem. Radiochem.*, 1967, **10**, 247.
22. a) K. D. Demadis, C. M. Hartshorn, T. J. Meyer, *Chem. Rev.*, 2001, **101**, 2655; b) R. F. Winter, *Organometallics*, 2014, **33**, 4517.
23. a) R. S. Threlkel, J. E. Bercaw, P. F. Seidler, J. M. Stryker, R. G. Bergman, *Org. Synth.,* 1993, **8**, 505; b) K. Fredenhagen, G. Cadenbach, *Z. Anorg. Allg. Chem.*, 1926, **158**, 249; c) C. Rüdorff, E. Schulze, *Z. Anorg. Allg. Chem.*, 1954, **277**, 156.
24. B. T. Loughrey, B. V. Cunning, P. C. Healy, C. L. Brown, P. G. Parsons, M. L. Williams, *Chem. Asian J.,* 2012, **7**, 112.
25. a) G. M. Sheldrick, *Acta Crystallogr.*, 2008, **A64**, 112; b) G. M. Sheldrick, *Acta Crystallogr.*, 2015, **A71**, 3.
26. A. L. Spek, *J. Appl. Cryst.* **2003**, *36*, 7.
27. M. J. Frisch, G. W. Trucks, H. B. Schlegel et al. *Gaussian 09*, Revision E.01, Gaussian, Inc., Wallingford CT, USA, 2009.‡
28. S. Grimme, J. Antony, S. Ehrlich, H. Krieg, *J. Chem. Phys.,* 2010, **132**, 154104.
29. a) A. D. Becke, *J. Chem. Phys.,* 1993, **98**, 5648; b) P. J. Stephens, F. J. Devlin, C. F. Chabalowski, M. J. Frisch, *J. Phys. Chem.,* 1994, **98**, 11623.
30. J. Tomasi, B. Mennucci, R. Cammi, *Chem. Rev.,* 2005, **105**, 2999.
31. GaussView 5.0.9: R. Dennington, T. A. Keith, J. M. Millam, Semichem Inc. Shawnee Mission, KS, 2016.

